

# Wirelessly charged AA battery with a curved receiving coil

Egor D. Demeshko,<sup>1</sup> Andrei A. Mineev,<sup>1</sup> Danil A. Chernomorov,<sup>1</sup> Oleg I. Burmistrov,<sup>1</sup> Alexey A. Dmitriev,<sup>1</sup> Sergey S. Ermakov,<sup>1</sup> Alina D. Rozenblit,<sup>1</sup> Pavel S. Seregin,<sup>1</sup> and Nikita A. Olekhno<sup>1, \*</sup>

<sup>1</sup>*School of Physics and Engineering, ITMO University,  
49 Kronverksky pr., bldg. A, 197101 Saint Petersburg, Russia*

(Dated: August 20, 2024)

Wireless power transfer is one of key drivers in modern consumer electronics, as it allows enhancing the convenience and usability of many devices. However, in most cases wireless charging is accessible only to devices developed with such a functionality in mind or at least to gadgets with standard charging connectors, such as USB type-C. We propose the design of a rechargeable battery having the size and output voltage characteristics of a standard AA battery, but supporting magnetic wireless power transfer from charging stations of widely used Qi standard. In our numerical simulations, we study the magnetic field distributions and scattering parameters of the introduced battery with a curved receiving coil coupled to a planar transmitting coil. The obtained results are supported by an experimental realization of the proposed design and a study of the prototype characteristics. The developed battery design facilitates the possibility of adding wireless charging functionality to a wide range of electronic devices in a universal way.

## I. INTRODUCTION

Wireless power transfer (WPT) [1] finds numerous applications both in the areas where it solves technical issues related to the presence of wires, brushes, or connectors providing power transmission, for example, in magnetic resonance imaging [2, 3], as well as in consumer devices where it allows enhancing the user comfort and device usability [4].

The types of electromagnetic near-field WPT are classified by the coupling mechanism between a transmitter and a receiver, which include capacitive [5], inductive [6], and magnetic resonant [7] couplings. The latter provides an efficient power transmission over greater distances compared to capacitive [8] and inductive [7] WPT due to a strong coupling between the transmitting and receiving coils sharing the same resonant frequency, and usually operates at kHz or MHz frequencies. Along with a conventional resonant WPT implementation via  $LC$ -circuits [7], various concepts for improving the WPT efficiency have been addressed, including applications of artificial composite medium [9–11] or high-index dielectric resonators [12]. Finally, long-range energy transmission over several meters and larger distances can be realized with the use of far-field microwave techniques [13, 14] and infrared lasers [15].

The key standard of magnetic resonant WPT for consumer electronics is Qi [16], which is widely used in smartphones, smart watches, earphones, power banks, and computer mice, to name a few. Qi transmitters are often integrated in public infrastructure, with the Internet of Things concepts being developed to optimize the usage of chargers [17]. Moreover, many promising industrial and medical applications of Qi undergo a phase of active development, including compact health track-

ing rings [18], electronic tattoos [19], and lab-on-a-chip centrifugal microfluidic platforms [20, 21]. Finally, Qi standard is applied in designing specific experimental setups such as swarms of tiny moving robots [22].

However, there is still a room for further improvement of Qi devices usability. One direction focuses on making the charging procedure itself more convenient, for example, by experimenting with the shape of charging stations [23], designing flexible embroidered [24, 25] and liquid metal [26] coils, or integrating transmitting WPT coils in clothes, such as recently reported charging glove [19, 26]. On the other hand, the most of modern Qi-receivers are connected to the devices being charged via USB Type-C, except for several solutions addressing specific gadgets, while the vast majority of electronic devices, e.g. those relying on standard AA batteries, still cannot be supplied with WPT receivers. This lack of universality sufficiently limits the applicability of wire-

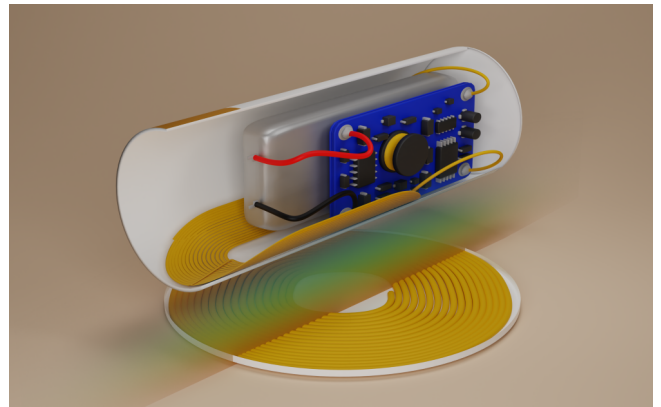


Figure 1. Concept of the proposed battery. The AA battery-sized module which includes a receiving coil (yellow), a receiver circuitry (blue printed circuit board), a rechargeable battery (grey), and a plastic casing (white) is placed atop the transmitting coil.

\* [nikita.olekhno@metalab.ifmo.ru](mailto:nikita.olekhno@metalab.ifmo.ru)

less charging in peripherals such as remote controls and computer mouses, toys, and other equipment not supplied with USB connectors.

In the present paper, we introduce a rechargeable battery having the size and output voltage characteristics corresponding to those of AA battery and incorporating a Qi standard receiving coil and a Li-ion cell, Fig. 1. By studying the proposed system numerically and experimentally, we demonstrate that such a scheme is feasible for further development of universal wireless charging solutions.

The paper is organized as follows. In Sec. II, we describe the structure of the proposed battery. Then, in Sec. III, we discuss numerical simulations of a curved, AA battery-sized receiving coil, evaluating its efficiency and studying the power transfer dependence on the receiving coil curvature, the distance between the receiving and transmitting coils, and the rotation angle of the receiving coil along the battery axis. Section IV considers experimental realization of the battery prototype, including scattering parameters and charge curve measurements. Section V contains a discussion of the obtained results and an outlook.

## II. STRUCTURE OF THE BATTERY

The proposed wirelessly charged battery includes the following components, depicted schematically in Fig. 1: (i) a plastic casing having the shape of a cylinder with diameter  $d = 14.5$  mm and length  $l = 50$  mm corresponding to the dimensions of a standard AA battery; (ii) two metallic contact pads, an anode and a cathode, at the top and bottom bases of the cylinder (not shown for visual clarity); (iii) Qi receiving coil which captures magnetic field created by a transmitting coil of a charging station; (iv) a receiver circuit which rectifies the ac voltage from the receiving coil and converts it to 5 V dc voltage, as well as performs the load modulation by switched bypassing the input  $LC$  circuit with two 22 nF capacitors to establish the connection with the transmitter and provide information transfer via the Qi protocol [27]; (v) a rechargeable Li-ion cell; and (vi) two dc-dc converters, one transforming the output voltage of the receiver circuit  $U_r = 5$  V to the rechargeable Li-ion cell charging voltage  $U_b = 3.8..4.2$  V and the other one transforming the rechargeable cell voltage to the output voltage  $U_{out} = 1.5$  V corresponding to the nominal value for AA batteries.

Typically, a receiver circuit in standard Qi receivers is implemented as a flexible printed circuit board (PCB), while the receiving coil is wound from an insulated wire and supplied with a flexible ferrite layer at the inner side (i.e., the one opposite to the transmitter location) to provide a magnetic shielding. Thus, an initially flat receiving coil can be bent around the inner surface of a plastic casing to fit into the AA battery shape, which is necessary if standard Qi receiving coils are used since the

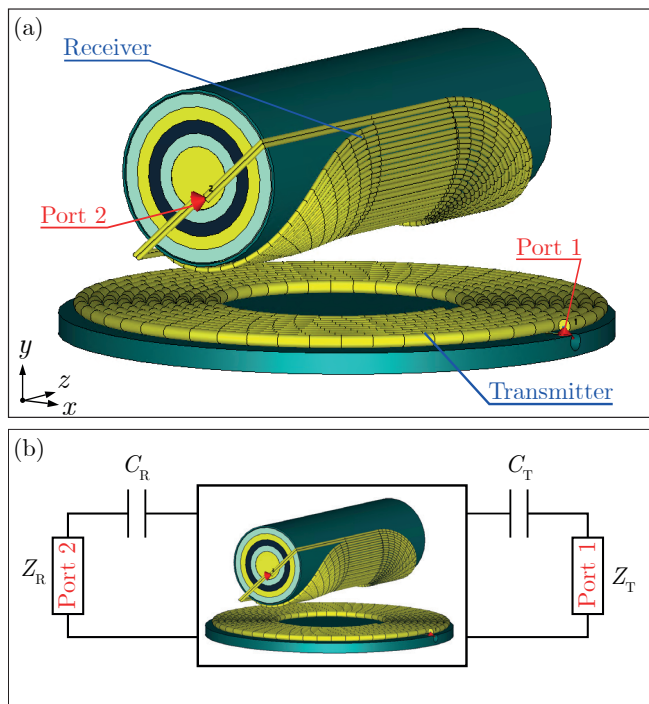


Figure 2. (a) Geometry of the numerical model which includes the receiving and transmitting coils, two ferrite layers attached to each coil, a layered core-shell cylinder emulating a Li-ion cell, receiving circuit and dc-dc converters, and Ports 1,2. (b) Schematic block for the considered model having the form of a two-port circuit. The transmitter and receiver circuits include capacitors  $C_T$ ,  $C_R$  and the port impedances  $Z_T$ ,  $Z_R$ , respectively.

typical in-plane dimensions of the coil are of the order of  $30 \times 40$  mm.

To address the proposed concept feasibility, we proceed with numerical simulations and experimental studies of curved receiving coils. In particular, we consider the effects of the coil curvature radius, its spatial separation from the transmitting coil, and its rotation along the battery axis on the WPT efficiency and magnetic field distributions.

## III. NUMERICAL STUDIES OF CURVED RECEIVING COILS

We perform all numerical simulations with CST Microwave studio applying finite element method (FEM) solver in the frequency domain. The model shown in Fig. 2(a) includes the receiving coil (top) and the transmitting coil (bottom) supplied with ferrite layers, as well as two ports: Port 1 for the transmitter and Port 2 for the receiver, correspondingly. Inside the outline of AA battery which is covered by the receiving coil, a layered cylinder with length 40 mm and diameter 13.4 mm is placed emulating electromagnetic properties of a Li-ion cell and required electronics [28]. Within the schematic

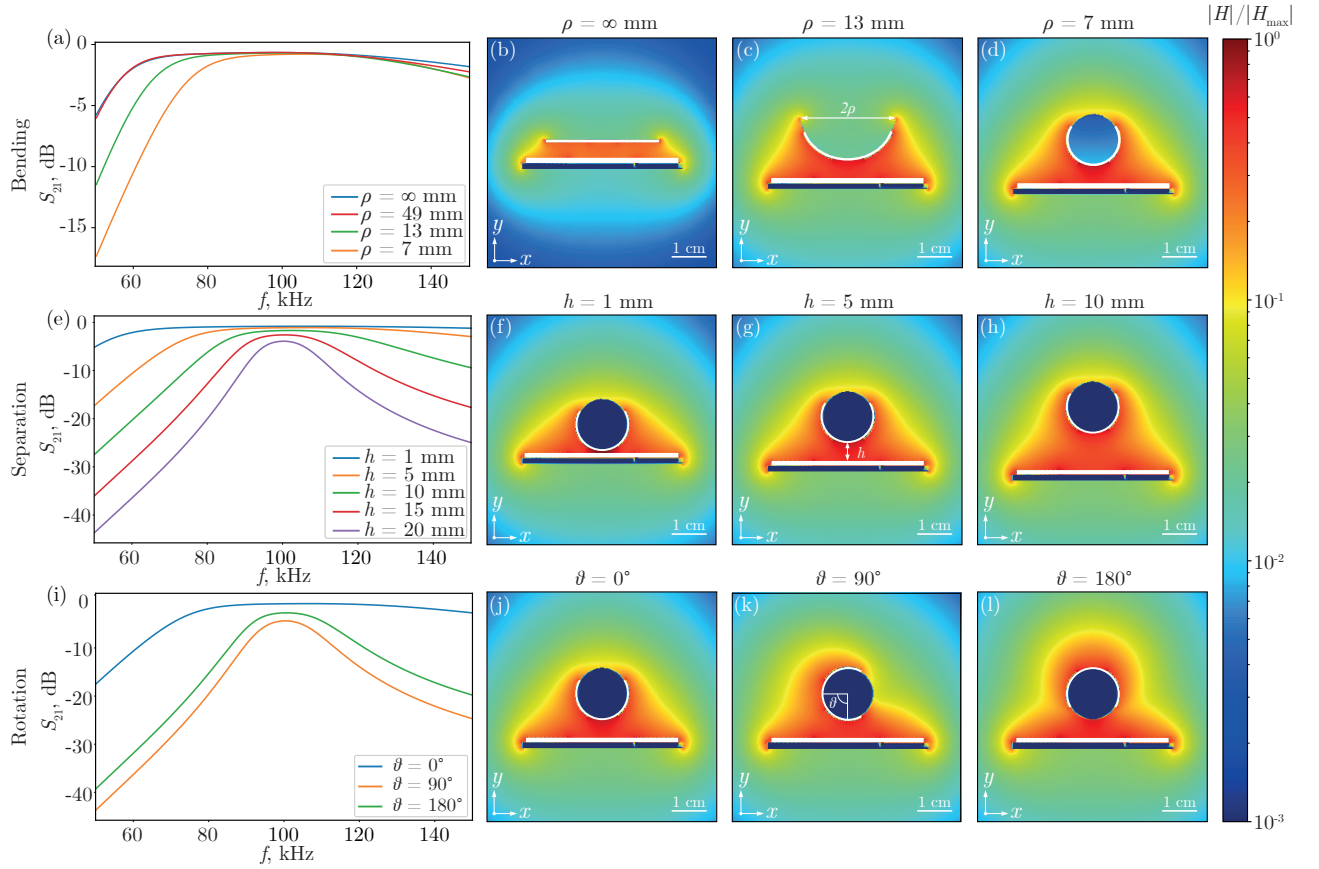


Figure 3. (a) Numerically calculated  $S_{21}$ -parameters for different values of curvature radius  $\rho$  of the receiving coil:  $\rho = \infty$  for a planar coil (blue),  $\rho = 49$  mm (red),  $\rho = 13$  mm (green), and  $\rho = 7$  mm corresponding to AA battery (orange). (b)-(d) Magnetic field profiles in the  $(xz)$ -plane passing through the battery midpoint for the receiving coils with curvature radii (b)  $\rho = \infty$ , (c)  $\rho = 13$  mm, and (d)  $\rho = 7$  mm, respectively. (e) Frequency dependencies of  $S_{21}$ -parameters for different distances  $h$  between a transmitting coil and a curved receiving coil ( $\rho = 7$  mm). (f)-(h) Magnetic field profiles in the  $(xz)$ -plane for (f)  $h = 1$  mm, (g)  $h = 5$  mm, and (h)  $h = 10$  mm. (i) Frequency dependencies of  $S_{21}$ -parameters for different receiving coil rotation angles  $\theta$ ;  $\rho = 7$  mm. (j)-(l) Magnetic field profiles in the  $(xz)$ -plane for (j)  $\theta = 0^\circ$ , (k)  $\theta = 90^\circ$ , and (l)  $\theta = 180^\circ$ .

block shown in Fig. 2(b), single capacitors  $C_T$  and  $C_R$  are attached in series with each coil to achieve a resonant coupling at  $f_0 = 100$  kHz. The port impedances  $Z_T$  and  $Z_R$  are matched, i.e. chosen in a way that guarantees that  $S_{11}$  and  $S_{22}$  are purely real and their amplitude does not exceed  $-30$  dB in the entire frequency range of consideration. The size of the simulation region is  $242 \times 242$  mm<sup>2</sup> in the  $(xz)$ -plane for all models in Fig. 3, while the size along the  $y$ -axis varies from 208 mm to 238 mm depending on the receiving coil curvature and its distance from the transmitting coil. Such dimensions of the simulation region provide sufficient simulation accuracy, as discussed in Supplemental Material [28] along with other details of numerical simulations and a description of the considered model with two coupled coils in the form of a T-circuit [25].

The outline of AA battery is a cylinder 49.5..50.5 mm in length with 13.7..14.5 mm diameter. Since the characteristic in-plane dimensions of a typical Qi receiving coil are  $30 \times 40$  mm, incorporating such a coil inside a AA

battery requires its bending. In turn, bending the coil changes the magnetic field distribution and the resonant frequency of the receiver [26, 29, 30].

We start with examining how a curvature radius  $\rho$  of the receiving coil bent around a cylindrical surface in the  $(xy)$ -plane in Fig. 2(a) affects the WPT efficiency. To proceed, we perform numerical simulations for the models with a flat receiving coil ( $\rho = \infty$ ), as well as for the receiving coils with curvature radii  $\rho = 49$  mm,  $\rho = 13$  mm, and  $\rho = 7$  mm, Fig. 3(a)-(d). The distance between the receiving and transmitting coils in all cases is  $h = 5$  mm, and the receiving coil is supplied with a thin ferrite layer [28]. As seen in Fig. 3(a), the  $S_{21}$ -parameters which characterize the transmission from the transmitting coil to the receiving coil demonstrate equal values in the vicinity of the considered resonant frequency  $f_0 = 100$  kHz, indicative of a nearly identical transmission efficiency independently of the receiving coil curvature, once a proper impedance matching is provided for the receiver and transmitter ports. However, despite

$S_{21}(f)$  dependencies for the flat receiving coil and the coil with a curvature radius  $\rho = 49$  mm demonstrate just a slight difference at high frequencies  $f > 120$  kHz [blue and red solid lines in Fig. 3(a)] while coinciding at the remaining frequencies, the curves for the receiving coils with  $\rho = 13$  mm and  $\rho = 7$  mm feature a considerably decreased coupling with a transmitting coil at low frequencies  $f = 50..80$  kHz compared to the flat receiving coil [green and orange solid lines in Fig. 3(a)]. The obtained results agree with Ref. [30] reporting a slight increase in the resonant frequency of curved coils resulting from a change in the coil inductance upon bending. A complementary problem – the dependence of charging efficiency on the transmitting coil curvature – has been addressed experimentally in Ref. [26] considering coils made of liquid GaInSn alloy.

The absolute values of magnetic field amplitude in the  $(xy)$ -plane  $H(x, y)$  are shown in Fig. 3(b)-(d) for  $\rho = \infty$ ,  $\rho = 13$  mm, and  $\rho = 7$  mm, respectively. It is seen that, intuitively, the magnetic field concentrates between the transmitting coil and the planar receiving coil homogeneously in Fig. 3(b), while forming a hot spot at the central region in Fig. 3(c) corresponding to the closest distance between the transmitting coil and the curved receiving coil with  $\rho = 13$  mm. Note that, despite the receiving coil is covered with a ferrite layer from the inner surface, the field is still present in the inner region of a cylindrical battery outline, which may lead to undesired couplings with other components if they are placed in the respective region. Finally, for the receiving coil with  $\rho = 7$  mm corresponding to AA battery dimensions and the ferrite layer forming a closed cylindrical surface, the magnetic field hot spot becomes more pronounced, while the field no longer penetrates in the inner region, Fig. 3(d). For both curved receiving coil geometries considered in Fig. 3(c,d), the magnetic field distribution in the surrounding free space changes inconsiderably, indicating that there should not arise any increased couplings with the environment or undesired electromagnetic fields acting on the user compared to the commercially available planar Qi receivers.

Next, we consider the dependence of scattering ( $S$ ) parameters and magnetic field distributions on the distance between the transmitting coil and the receiving coil with a curvature radius  $\rho = 7$  mm. As seen in Fig. 3(e), larger distances between the coils correspond to lower values of  $S_{21}$ -parameters, i.e., to lower transmission. Moreover, the out-of-resonance  $S_{21}$  values demonstrate an especially rapid decrease with distance. Since the Qi standard uses tuning out of the resonance as a means of regulation of the power transferred to the receiver, this rapid decrease might require special considerations while designing the software controlling the receiver-to-transmitter feedback, to prevent oscillations from appearing in the feedback loop. Magnetic field distributions shown in Fig. 3(f)-(h) demonstrate a vertical elongation of the field concentration region between the nearest points of the transmitting and receiving coils upon increasing the separation

$h$  from 1 mm to 10 mm, with a constriction in the field distribution formed for  $h = 10$  mm in Fig. 3(h) caused by the field localization near the coils' surfaces. Nevertheless, the magnetic field profile at the distances of several centimeters from the transmitting and receiving coils remains nearly unchanged.

Finally, we examine the influence of the receiving coil rotation with respect to the transmitting coil. Indeed, in a realistic application scenario, the user may place the battery in a device without any specific angular alignment. Figure 3(i) demonstrates  $S_{21}$ -parameters for three basic configurations corresponding to the rotation angles  $\theta = 0^\circ$ ,  $\theta = 90^\circ$ , and  $\theta = 180^\circ$ . It is seen that the system with the receiving coil rotated by  $\theta = 180^\circ$  demonstrates a considerably lower transmission coefficient compared to the basic configuration with  $\rho = 7$  mm,  $h = 5$  mm, and  $\theta = 0^\circ$ . Moreover, the corresponding  $S_{21}$  curve closely resembles the one in Fig. 3(e) for  $h = 15$  mm and  $\theta = 0^\circ$ , facilitating that a possible explanation of the lower transmission is an increase in the effective distance between the transmitting and receiving coils. As shown in Fig. 3(j,l), the magnetic field concentrates in the vicinity of the receiving coil, leading to a hot spot emergence at the opposite side of the battery in Fig. 3(l). However, the lowest transmission is observed for  $\theta = 90^\circ$ , as seen in Fig. 3(i). Qualitatively, a considerable part of the receiving coil surface becomes orthogonal to the transmitting coil plane, and thus parallel to the magnetic field direction, which results in lower coupling between the coils. In contrast to previous cases, magnetic field profiles for  $\theta = 90^\circ$  demonstrate a pronounced asymmetry in the vicinity of the receiving coil, see Fig. 3(k).

#### IV. EXPERIMENTAL RESULTS

We start the experimental studies with examining the dependence of  $S$ -parameters of the coupled transmitting and receiving coils. To perform the  $S$ -parameter measurement, the setup shown in Fig. 4(a) was used. It features two SMA connectors (1) and (6) used for connecting the setup to the output and input ports of a vector network analyzer (VNA), PCBs (2) and (5) with tank circuit capacitors and jumper terminals, the transmitting coil (3), and the receiving coil (4). Transmitter and receiver parts of the setup are both mounted on radio-transparent extruded polystyrene foam (XPS) foundations (8) which can be moved along one direction to vary the distance  $h$  between the receiving and transmitting coils.

The transmitting coil (3) is a planar spiral coil consisting of 10 turns of PTFE-insulated stranded copper wire with 1 mm diameter (the outer diameter of the coil is 42 mm, the inner diameter is 22 mm) placed on a disk-shaped ferrite layer with 45.5 mm diameter and 0.8 mm thickness. The capacitor (2) used with the transmitting coil is a single CBB21-404J-100V polypropylene film capacitor with a nominal capacitance of  $400 \text{ nF} \pm 5\%$ . Both the transmitting coil (3) and the capacitor (2) have been

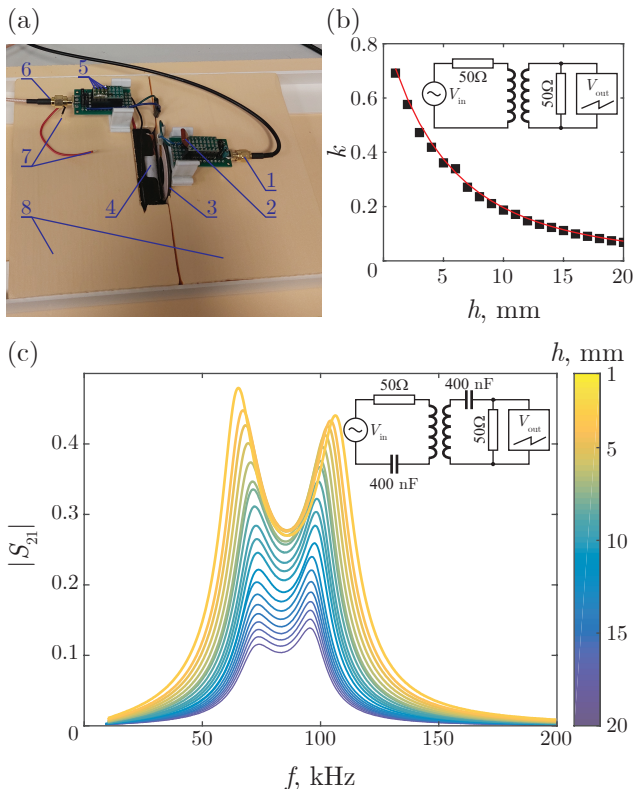


Figure 4. (a) Experimental setup for  $S$ -parameters measurement, consisting of (1) the VNA output port, (2) a 400 nF polymer film capacitor which can be assembled into a serial or parallel  $LC$ -circuit with the transmitting coil or bypassed using jumpers, (3) the transmitting coil, (4) the receiving coil inside a AA battery-sized photopolymer resin casing mounted inside a AA battery holder, (5) four ceramic capacitors 68 nF each connected in parallel which can be assembled into a serial or parallel  $LC$ -circuit with the receiving coil or bypassed using jumpers, and (6) the VNA input port. Battery holder output leads (7) are attached to provide the battery output voltage measurement. The setup is mounted on radio-transparent extruded polystyrene foam foundation (8) which can be moved in one direction to change the distance  $h$  between the receiving and transmitting coils. (b) The coil-to-coil coupling  $k$  dependence on the distance  $h$  between the transmitting and receiving coils. The circuit diagram is shown in the inset. (c) Experimentally measured dependence of  $S_{21}$ -parameters on the distance between the transmitting and receiving coils varied in the range from 1 to 10 mm. The inset shows the circuit diagram.

extracted from a disassembled Qi charger.

The receiver coil is a planar coil in the shape of a rounded rectangle with a 40.5 mm length and 30.5 mm width, consisting of 14 turns of a wire made of two parallel monolithic enameled copper conductors with a circular cross-section and a diameter of 0.4 mm, which are soldered together at their ends, with an inner  $22.5 \times 10.5$  mm<sup>2</sup> empty space. The coil is bent around a cylindrical surface with axis parallel to the coil's large side

and the curvature radius  $\rho = 7$  mm. Then, the coil is enclosed in a AA battery-sized casing manufactured using Anycubic Photon SLA 3D printer and backed with a  $41 \times 28$  mm<sup>2</sup> flexible ferrite sheet with 0.1 mm thickness from the interior side. As seen from the numerical simulations [28], the presence of components inside the battery does not considerably change the field distributions and  $S$ -parameters due to the magnetic field shielding by a ferrite layer. To confirm this, a Robiton 10440-sized 350 mAh Li-ion cell was installed inside the battery casing to simulate the presence of the aforementioned components. The casing containing the coil was installed into a AA battery holder mounted on a movable XPS foundation. The receiver tank capacitor assembly (5) consists of four Murata GRM31C5C1H104JA01L C0G ceramic capacitors, each having  $100$  nF  $\pm 5\%$  capacitance, connected in parallel, adding up to a total capacitance of 400 nF.

The capacitors beside both the receiving and the transmitting coils were mounted on PCBs that also housed the SMA connectors and the jumper terminals, which allow one to assemble a serial  $LC$  circuit, a parallel  $LC$  circuit, or to connect the coil directly to the port, depending on the jumper placement.

We start with considering the leakage inductances  $L_1$  of the transmitting and  $L_2$  of the receiving coil brought together to the distance  $h$  and their mutual inductance  $M$ . From the  $S$ -parameters obtained by connecting the coils directly to the VNA ports (50 Ohm impedance) as shown in the inset of Fig. 4(b), one can obtain the values of the self-inductances and the mutual inductance, as well as the corresponding resistances. The complete procedure is described in detail in Supplemental Material [28]. With the distance  $h$  varied from 1 to 20 mm, this procedure reveals a transmitting coil self-inductance  $L_{Tx} = L_1 + aM = 7$   $\mu$ H, where  $a = \frac{10}{14}$  is the winding turns ratio, and the receiving coil self-inductance  $L_{Rx} = L_2 + M/a = 12$   $\mu$ H. The coupling  $k = M/\sqrt{L_1 L_2}$  demonstrates a hyperbolic dependency  $k = [(h + h_0)/h_1]^{-\alpha}$  on the distance  $h$ , which is shown in Fig. 4(b). A least square fit yields the following parameter values:  $h_0 = 16.5$  mm,  $h_1 = 15.7$  mm,  $\alpha = 3.1$ .

Next, we add capacitors to the transmitting and the receiving coils and study the  $S$ -parameters of the resulting coupled serial  $LC$  circuits. Figure 4(c) shows the dependence of the transmission coefficient  $S_{21}$  from the transmitting coil to the receiving coil while the distance  $h$  is varied from 1 mm to 20 mm. First, it is seen that there are two clearly resolved resonant peaks in the dependence of  $|S_{21}|(f)$  on the frequency  $f$ . Their frequencies change considerably with the distance  $h$  between the coils at low distances, but eventually saturate at greater spacings, see Fig. 4(c). The appearance of a coupling-dependent resonant peak splitting indicates a hybridization of individual coils' resonant states, characteristic of strong-coupling regime [31]. Such systems typically display a fork-like dependence of the resonant frequencies on the coupling strength, with the transition to the weak-coupling regime marked by merging of two resonances into one. In our

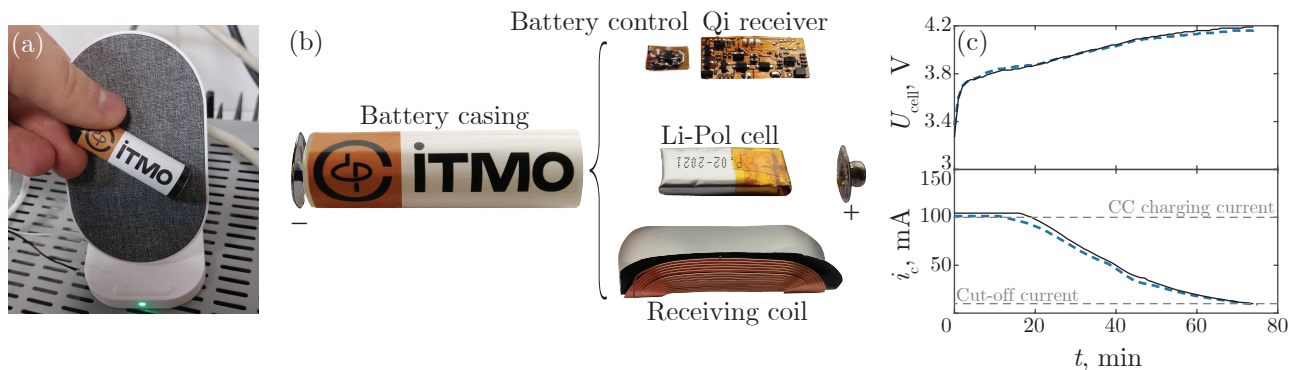


Figure 5. (a) Photo of the battery prototype placed atop a Qi charging station (gray). Green lit LED indicates a correctly established connection and ongoing charging process. (b) Exploded-view diagram of the experimental prototype featuring photographs of the photopolymer resin casing, positive (+) and negative (-) battery terminals, the Li-ion rechargeable cell (Li-ion cell), the receiving coil with a ferrite layer (Receiving coil), a flexible circuit board containing the standard Qi receiver (Qi receiver) and a flexible circuit board containing STC4054 Li-ion cell charge controller chip and the 1.5 V output dc-dc converter (Battery control). (c) Measured time dependence of the Li-ion cell voltage  $V_{\text{cell}}$  and charge current  $i_c$  for the prototype placed atop a 10 W Qi charging station.

case, however, the  $LC$  circuits have different resonant frequencies (100 kHz for the transmitting coil and 70 kHz for the receiving one). Thus, rather than a splitting, the distance dependency of the resonant frequencies demonstrates an anticrossing, which is yet another manifestation of the strong coupling regime [32]. Note that only the decreasing region of the high-frequency resonant peak is used for power transmission to monotonously tune the transmission rate with frequency according to the Qi standard [27].

To demonstrate the practical applicability of our concept, we assemble a battery prototype shown in Fig. 5(a). The prototype demonstrates a Qi-compatible load modulation carrying packets that are recognized by a standard Qi charging station (the fabric-covered pad under the battery prototype) allowing them to establish a connection, which is indicated by a green-lit LED at the transmitter in Fig. 5(a). The prototype exploded-view diagram composed of actual photographs of its components is shown in Fig. 5(b). The prototype includes the following parts: (i) a casing having the shape of an empty cylinder with the height of 47.8 mm, the diameter of 14 mm, and the wall thickness of 0.5 mm made of photopolymer resin at the Anycubic Photon SLA 3D printer; (ii) metallic contact pads; (iii) a  $40.5 \times 30.5 \text{ mm}^2$  curved receiving coil identical to that used in the  $S$ -parameters measurements; (iv) a flexible ferrite layer attached to the coil; (v) the Qi receiver circuit; (vi) the PCB with a battery charger based on the dissipative voltage-current regulator STC4054 which converts 5 V output voltage from Qi receiver circuit to a suitable charging voltage for the Li-ion cell (100 mA current in the constant-current mode and 4.2 V in the constant-voltage mode) and a dc-dc converter transforming the Li-ion cell voltage to 1.5 V at the battery output; (vii) the Go Power LP451124 65 mAh Li-ion cell.

To evaluate the time needed to fully charge the battery

using WPT, we obtained its charge curves with the assembled battery placed atop a 10 W Qi-compatible charging station. An ammeter was plugged into the plus cable of the Li-ion cell, while a voltmeter was connected to the positive and negative leads of the cell. The obtained curves are shown with solid lines in Fig. 5(c). The first 17 minutes correspond to the constant-current (CC) charging mode at  $i_{\text{CC}} = 100$  mA, which is characterized by a rapid voltage increase. After that, the STC4054 chip performed a transition to the constant-voltage (CV) mode, which is characterized by a gradual current decrease accompanying a slow voltage increase. After 75 minutes of charging, the current falls below the cut-off current, which is defined as  $0.1i_{\text{CC}}$ , at which point the charging is considered complete and the STC4054 chip disconnects the cell from the charging source. For comparison, charge curves have also been obtained for a planar received coil in the shape of a rounded rectangle with a 40.5 mm length and 30.5 mm width, 14 turns of a wire consisting of two parallel monolithic enameled copper conductors with a circular cross-section and a diameter of 0.4 mm, which are soldered together at their ends, with an inner  $22.5 \times 10.5 \text{ mm}^2$  empty space, placed atop the same charging station and connected to receiver circuitry identical to that used in the battery prototype. The resulting charge curves shown with dashed lines in Fig. 5(c) demonstrate no significant difference compared to our prototype with a curved receiving coil.

## V. CONCLUSION AND OUTLOOK

To conclude, we have proposed the concept of a wirelessly charged battery having the parameters of a standard AA battery and supplied with a curved Qi receiving coil. Examining the proposed concept numerically and experimentally, we demonstrate that the application of a

receiving coil bent around the inner side of a cylindrical battery casing provides sufficient coupling to implement wireless charging and demonstrates WPT efficiency close to that of a standard receiver with a planar coil. We also address the effects of battery rotation around its symmetry axis and spatial separation between the battery and the transmitting coil. Finally, we validate the concept experimentally by constructing a fully operational prototype.

The directions of further development are the following. First, the considered proof-of-concept design can be enhanced from the engineering point of view by employing more advanced rechargeable batteries to provide higher power density [33], constructing receiving coils based on novel approaches such as liquid metal and textile-based ones [24–26], implementing the features introduced in the Qi2 standard, and developing custom electronic circuits to make them more compact, thus providing more space for a rechargeable cell. Second, various physical effects should be considered, such as interactions between several receivers [34–37], corresponding in our

case to powering up a certain device with several wirelessly charged batteries simultaneously. Finally, there are several WPT concepts and standards under active development, which include room-scale volumetric wireless charging working at frequencies from 1 MHz [37] to 1.34 MHz [38]. Developing a wirelessly charged battery compatible simultaneously with any of the mentioned standards and Qi renders feasible, see the example for a composite Qi-AirFuel transmitter [39], yet very interesting task, capable of bringing a truly universal wireless charging solutions.

## ACKNOWLEDGMENTS

We acknowledge fruitful discussions with Eugen Koshin and Aigerim Jandaliyeva. The work was supported by state assignment No. FSER-2024-0041 within the framework of the national project "Science and Universities".

- 
- [1] Takehiro Imura, *Wireless Power Transfer: Using Magnetic and Electric Resonance Coupling Techniques* (Springer Singapore, 2020).
  - [2] Lena Nohava, Jean-Christophe Ginefri, Georges Willoquet, Elmar Laistler, and Roberta Frass-Kriegel, "Perspectives in wireless radio frequency coil development for magnetic resonance imaging," *Frontiers in Physics* **8**, 11 (2020).
  - [3] Oleg I Burmistrov, Nikita V Mikhailov, Dmitriy S Dashkevich, Pavel S Seregin, and Nikita A Olekhno, "Wireless power transfer in magnetic resonance imaging at a higher-order mode of a birdcage coil," *Physical Review Applied* **21**, 014047 (2024).
  - [4] Aisha Alabsi, Ammar Hawbani, Xingfu Wang, Ahmed Al-Dubai, Jiankun Hu, Samah Abdel Aziz, Santosh Kumar, Liang Zhao, Alexey V Shvetsov, and Saeed Hamood Alsamhi, "Wireless power transfer technologies, applications, and future trends: A review," *IEEE Transactions on Sustainable Computing* (2024), 10.1109/TSUSC.2024.3380607.
  - [5] Fei Lu, Hua Zhang, and Chris Mi, "A review on the recent development of capacitive wireless power transfer technology," *Energies* **10**, 1752 (2017).
  - [6] Grant A Covic and John T Boys, "Inductive power transfer," *Proceedings of the IEEE* **101**, 1276–1289 (2013).
  - [7] Andre Kurs, Aristeidis Karalis, Robert Moffatt, John D Joannopoulos, Peter Fisher, and Marin Soljacic, "Wireless power transfer via strongly coupled magnetic resonances," *Science* **317**, 83–86 (2007).
  - [8] Jiejian Dai and Daniel C Ludois, "A survey of wireless power transfer and a critical comparison of inductive and capacitive coupling for small gap applications," *IEEE Transactions on Power Electronics* **30**, 6017–6029 (2015).
  - [9] Bingnan Wang, Koon Hoo Teo, Tamotsu Nishino, William Yerazunis, John Barnwell, and Jinyun Zhang, "Experiments on wireless power transfer with metamaterials," *Applied Physics Letters* **98** (2011).
  - [10] Guy Lipworth, Joshua Ensworth, Kushal Seetharam, Da Huang, Jae Seung Lee, Paul Schmalenberg, Tsuyoshi Nomura, Matthew S Reynolds, David R Smith, and Yaroslav Urzhumov, "Magnetic metamaterial superlens for increased range wireless power transfer," *Scientific Reports* **4**, 3642 (2014).
  - [11] Erik Saturnino Gámez Rodríguez, Anil Kumar Ram-Rakhyani, David Schurig, and Gianluca Lazzi, "Compact low-frequency metamaterial design for wireless power transfer efficiency enhancement," *IEEE Transactions on Microwave Theory and Techniques* **64**, 1644–1654 (2016).
  - [12] Wei Wang, Simon Hemour, and Ke Wu, "Coupled resonance energy transfer over gigahertz frequency range using ceramic filled cavity for medical implanted sensors," *IEEE transactions on microwave theory and techniques* **62**, 956–964 (2014).
  - [13] Kyo D Song, Jaehwan Kim, Jung W Kim, Yeonjoon Park, Jay J Ely, Hyun J Kim, and Sang H Choi, "Preliminary operational aspects of microwave-powered airship drone," *International Journal of Micro Air Vehicles* **11**, 1756829319861368 (2019).
  - [14] Ricardo AM Pereira and Nuno Borges Carvalho, "Quasioptics for increasing the beam efficiency of wireless power transfer systems," *Scientific Reports* **12**, 20894 (2022).
  - [15] Qingqing Zhang, Wen Fang, Qingwen Liu, Jun Wu, Pengfei Xia, and Liuqing Yang, "Distributed laser charging: A wireless power transfer approach," *IEEE Internet of Things Journal* **5**, 3853–3864 (2018).
  - [16] Shu Yuen Ron Hui, "Planar wireless charging technology for portable electronic products and Qi," *Proceedings of the IEEE* **101**, 1290–1301 (2013).
  - [17] Kuan-Ting Lai, Fu-Chiung Cheng, Seng-Cho T Chou, Yi-Chun Chang, Guo-Wei Wu, and Jung-Cheng Tsai,

- “AnyCharge: An IoT-based wireless charging service for the public,” *IEEE Internet of Things Journal* **6**, 10888–10901 (2019).
- [18] Son Nguyen, Connie Duong, and Rajeevan Amirtharajah, “A smart health tracking ring powered by wireless power transfer,” in *2021 IEEE Wireless Power Transfer Conference (WPTC)* (IEEE, 2021) pp. 1–4.
- [19] Nanshu Lu, Sangjun Kim, Jonathan Wells, Sarnab Bhattacharya, Hamsi Nathan, Jiaming He, Isabella Tubilla, Heeyong Huh, Pooja Kakani, Ali Farshkaran, *et al.*, “A wearable and unobstructive Qi-compatible wireless charger,” (2023), [10.21203/rs.3.rs-3509616/v1](https://arxiv.org/abs/2023.03.3509616v1).
- [20] Saraí M Torres Delgado, David J Kinahan, Fralett Suárez Sandoval, Lourdes Albina Nirupa Julius, Niamh A Kilcawley, Jens Ducrée, and Dario Mager, “Fully automated chemiluminescence detection using an electrified-Lab-on-a-Disc (eLoaD) platform,” *Lab on a Chip* **16**, 4002–4011 (2016).
- [21] Saraí M Torres Delgado, David J Kinahan, Lourdes Albina Nirupa Julius, Adam Mallette, David Sáenz Ardila, Rohit Mishra, Celina M Miyazaki, Jan G Korvink, Jens Ducrée, and Dario Mager, “Wirelessly powered and remotely controlled valve-array for highly multiplexed analytical assay automation on a centrifugal microfluidic platform,” *Biosensors and Bioelectronics* **109**, 214–223 (2018).
- [22] Shengkai Li, Bahnisikha Dutta, Sarah Cannon, Joshua J Daymude, Ram Avinery, Enes Aydin, Andréa W Richa, Daniel I Goldman, and Dana Randall, “Programming active cohesive granular matter with mechanically induced phase changes,” *Science Advances* **7**, eabe8494 (2021).
- [23] Seong-Min Kim, In-Kui Cho, Sang-Won Kim, Jung-Ick Moon, and Ho-Jin Lee, “A Qi-compatible wireless charging pocket for smartphone,” in *2020 IEEE Wireless Power Transfer Conference (WPTC)* (IEEE, 2020) pp. 387–390.
- [24] Danmei Sun, Meixuan Chen, Symon Podilchak, Apostolos Georgiadis, Qassim S Abdullahi, Rahil Joshi, Sohail Yasin, Jean Rooney, and John Rooney, “Investigating flexible textile-based coils for wireless charging wearable electronics,” *Journal of industrial textiles* **50**, 333–345 (2020).
- [25] Sebastian Micus, Laura Padani, Michael Haupt, and Götz T Gresser, “Textile-based coils for inductive wireless power transmission,” *Applied Sciences* **11**, 4309 (2021).
- [26] Long Teng, Lifei Zhu, Stephan Handschuh-Wang, and Xuechang Zhou, “Robust, multiscale liquid-metal patterning enabled by a sacrificial sealing layer for flexible and wearable wireless powering,” *Journal of Materials Chemistry C* **7**, 15243–15251 (2019).
- [27] Dries Van Wageningen and Toine Staring, “The Qi wireless power standard,” in *Proceedings of 14th International Power Electronics and Motion Control Conference EPE-PEMC 2010* (IEEE, 2010) pp. S15–25.
- [28] See Supplemental Material at [URL] for (i) the details of numerical simulations; (ii) a comparison of different receiving coil designs; (iii) circuit schematics of the prototype; (iv) the description of experimental techniques.
- [29] Kartik Sondhi, Nicolas Garraud, Daniel Alabi, David P. Arnold, Alexandra Garraud, Sai Guruva Reddy Avuthu, Hugh Z. Fan, and Toshikazu Nishida, “Flexible screen-printed coils for wireless power transfer using low-frequency magnetic fields,” *Journal of micromechanics and microengineering* **29**, 084006 (2019).
- [30] Lulu Xu, Xiao Chen, Sirui Tan, Zhirun Hu, Baoan Ying, Terry Tao Ye, and Yi Li, “Characterization and modeling of embroidered NFC coil antennas for wearable applications,” *IEEE Sensors Journal* **20**, 14501–14513 (2020).
- [31] G. Khitrova, H. M. Gibbs, M. Kira, S. W. Koch, and A. Scherer, “Vacuum Rabi splitting in semiconductors,” *Nature Physics* **2**, 81–90 (2006).
- [32] Hui Cao and Jan Wiersig, “Dielectric microcavities: Model systems for wave chaos and non-hermitian physics,” *Reviews of Modern Physics* **87**, 61–111 (2015).
- [33] James T. Frith, Matthew J. Lacey, and Ulderico Ulissi, “A non-academic perspective on the future of lithium-based batteries,” *Nature Communications* **14** (2023), [10.1038/s41467-023-35933-2](https://doi.org/10.1038/s41467-023-35933-2).
- [34] Minfan Fu, Tong Zhang, Chengbin Ma, and Xinen Zhu, “Efficiency and optimal loads analysis for multiple-receiver wireless power transfer systems,” *IEEE Transactions on Microwave Theory and Techniques* **63**, 801–812 (2015).
- [35] Minfan Fu, Tong Zhang, Xinen Zhu, Patrick Chi-Kwong Luk, and Chengbin Ma, “Compensation of cross coupling in multiple-receiver wireless power transfer systems,” *IEEE Transactions on Industrial Informatics* **12**, 474–482 (2016).
- [36] Pavel Smirnov, Eugene Koreshin, Georgii Baranov, and Polina Kapitanova, “Self-tuning approach for metasurface-based resonators for one-to-many wireless power transfer,” *Journal of Applied Physics* **134** (2023), [10.1063/5.0152710](https://doi.org/10.1063/5.0152710).
- [37] Nikita Mikhailov, Marina Abrosimova, Aigerim Jandaliyeva, Mikhail Sigantov, Pavel Belov, and Alena Shchelokova, “Multi-object charging in room-sized weakly coupled WPT system,” in *2024 IEEE Wireless Power Technology Conference and Expo (WPTCE)* (IEEE, 2024) pp. 364–367.
- [38] Takuya Sasatani, Alanson P Sample, and Yoshihiro Kawahara, “Room-scale magnetoquasistatic wireless power transfer using a cavity-based multimode resonator,” *Nature Electronics* **4**, 689–697 (2021).
- [39] Elisabetta Moisello, Alberto Cattani, Piero Malcovati, and Edoardo Bonizzoni, “A wireless power transfer antenna and active rectifier system compatible with Qi and AirFuel standards,” in *2024 International Symposium on Power Electronics, Electrical Drives, Automation and Motion (SPEEDAM)* (IEEE, 2024) pp. 930–935.



# Supplemental Material

## Wirelessly charged AA battery with a curved receiving coil

Egor D. Demeshko,<sup>1</sup> Andrei A. Mineev,<sup>1</sup> Danil A. Chernomorov,<sup>1</sup> Oleg I. Burmistrov,<sup>1</sup> Alexey A. Dmitriev,<sup>1</sup>  
Sergey S. Ermakov,<sup>1</sup> Alina D. Rozenblit,<sup>1</sup> Pavel S. Seregin,<sup>1</sup> and Nikita A. Olekhno<sup>1, \*</sup>

<sup>1</sup>*School of Physics and Engineering, ITMO University,  
49 Kronverksky pr., bldg. A, 197101 Saint Petersburg, Russia*

(Dated: August 20, 2024)

### CONTENTS

Supplementary Note 1. Numerical simulations	1
Supplementary Note 2. Comparison of receiving coils	3
Supplementary Note 3. Experimental setups	4
Supplementary Note 4. Prototype schematics	8
References	9

### SUPPLEMENTARY NOTE 1. NUMERICAL SIMULATIONS

We start with constructing numerical models of the transmitting and a receiving coils with geometries corresponding to those widely applied in Qi-standard wireless power transfer (WPT) using CST Microwave Studio. The transmitting coil is implemented as a spiral circular coil having 10 turns of a circular cross-section copper wire with diameter 0.4 mm and 0.1 mm turn spacing. The outer diameter of the transmitting coil reaches 40 mm. To enhance the magnetic coupling, the transmitter is placed atop the ferrite substrate with the diameter 42 mm and the height 1.6 mm.

The receiving coil model represents a rectangular-shaped spiral inductor with 14 turns of a wire consisting of two parallel copper conductors, with the diameter of a single wire being 0.4 mm. The turn spacing is 0.06 mm, and the overall in-plane dimensions of the coil are  $40 \times 30$  mm. The receiving coil is also supplied with a ferrite layer having the thickness of 0.2 mm. Within numerical simulations described in the main text, the receiving coil geometry varies from a flat coil to cylindrical surfaces with different curvature radii  $\rho$ .

The receiving and the transmitting coils are surrounded by vacuum media. The wire material is copper, characterized by the electric conductivity  $\sigma = 5.96 \times 10^7$  S/m as defined in the CST Microwave Studio materials library. For the ferrite substrates, we set the following material properties: permittivity  $\varepsilon = 1$  and permeability  $\mu = 2000$ . To emulate the presence of a Li-ion cell, printed circuit boards (PCBs), and wires in the inner region surrounded by the receiving coil, we place a multilayered core-shell cylinder in this area with the following layer parameters: a ferrite layer with  $D_{\text{out}} = 13.4$  mm and  $D_{\text{in}} = 13.0$  mm, the first aluminum layer with  $D_{\text{out}} = 12.8$  mm and  $D_{\text{in}} = 10.8$  mm,

---

\* [nikita.olekhno@metalab.ifmo.ru](mailto:nikita.olekhno@metalab.ifmo.ru)

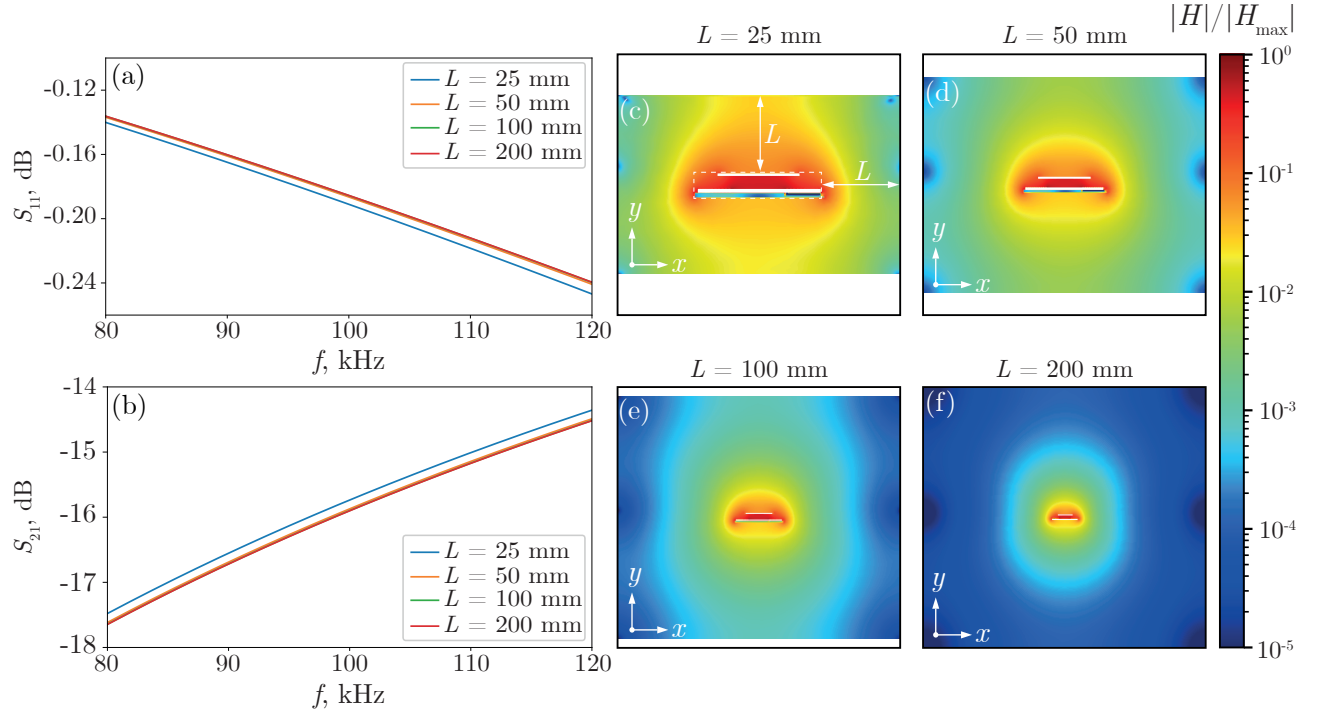


Figure S1. Comparison of numerical results for different simulation region sizes. (a) Frequency dependencies of  $S_{11}$ -parameters for several values of the offset  $L$  between the edges of transmitting and receiving coils and the simulation region boundaries: 25 mm, 50 mm, 100 mm, and 200 mm. (b) The same as panel (a), but for  $S_{21}$ -parameters. (c)-(f) Magnetic field profiles in the  $(xy)$ -plane for the simulation box offsets (c) 25 mm, (d) 50 mm, (e) 100 mm, and (f) 200 mm, respectively. The distance between the transmitting coil and the planar receiving coil is  $h = 5$  mm.

a copper layer with  $D_{\text{out}} = 10.8$  mm and  $D_{\text{in}} = 8.8$  mm, a graphite layer with  $D_{\text{out}} = 8.8$  mm and  $D_{\text{in}} = 6.8$  mm, the second aluminum layer with  $D_{\text{out}} = 6.8$  mm and  $D_{\text{in}} = 4.8$  mm, and a copper core with  $D_{\text{out}} = 4.8$  mm.

For Qi WPT operating at frequencies 100–200 kHz, the wavelength ranges from one and a half to three kilometers, which, taken together with characteristic receiving and transmitting coils feature sizes of several millimeters, complicates the consideration of simulation regions exceeding the wavelength. To establish the optimal simulation region size, we perform numerical calculations of  $S_{11}$ - and  $S_{21}$ -parameters and magnetic field distributions for the same configuration including the transmitting coil and the flat receiving coil separated by a 5 mm gap, and change the offset  $L$  between the model's edges and boundaries implemented as perfectly matched layers. The obtained results for  $S_{11}$ - and  $S_{21}$ -parameters demonstrate that  $S$ -parameters differ for  $L = 25$  mm and  $L = 50$  mm, but saturate and become hardly resolvable for the offsets  $L = 50$  mm,  $L = 100$  mm, and  $L = 200$  mm, see Fig. S1(a,b). Moreover, magnetic fields do not considerably vanish near the simulation region boundaries for the offsets  $L = 25$  mm and  $L = 50$  mm [Fig. S1(c,d)], while for larger offsets  $L = 100$  mm and  $L = 200$  mm the magnetic field amplitudes at the boundaries are  $10^3$  and  $10^4$  times lower than the maximal values for the simulated models, correspondingly, Fig. S1(e,f). To find a balance between the calculation accuracy and the calculation time, the offset  $L = 100$  mm has been selected for further simulations, which corresponds to the overall simulation region sizes around  $242 \times 242 \times 200$  mm<sup>3</sup>. Note that for the described simulations we do not add a serial capacitance to the coils, therefore frequency dependencies of  $S_{11}$ - and  $S_{21}$ -parameters do not feature any resonances in the vicinity of  $f = 100$  kHz.

Next, we address the effects of components such as Li-ion cell, PCBs, and wires placed near the receiving coil on

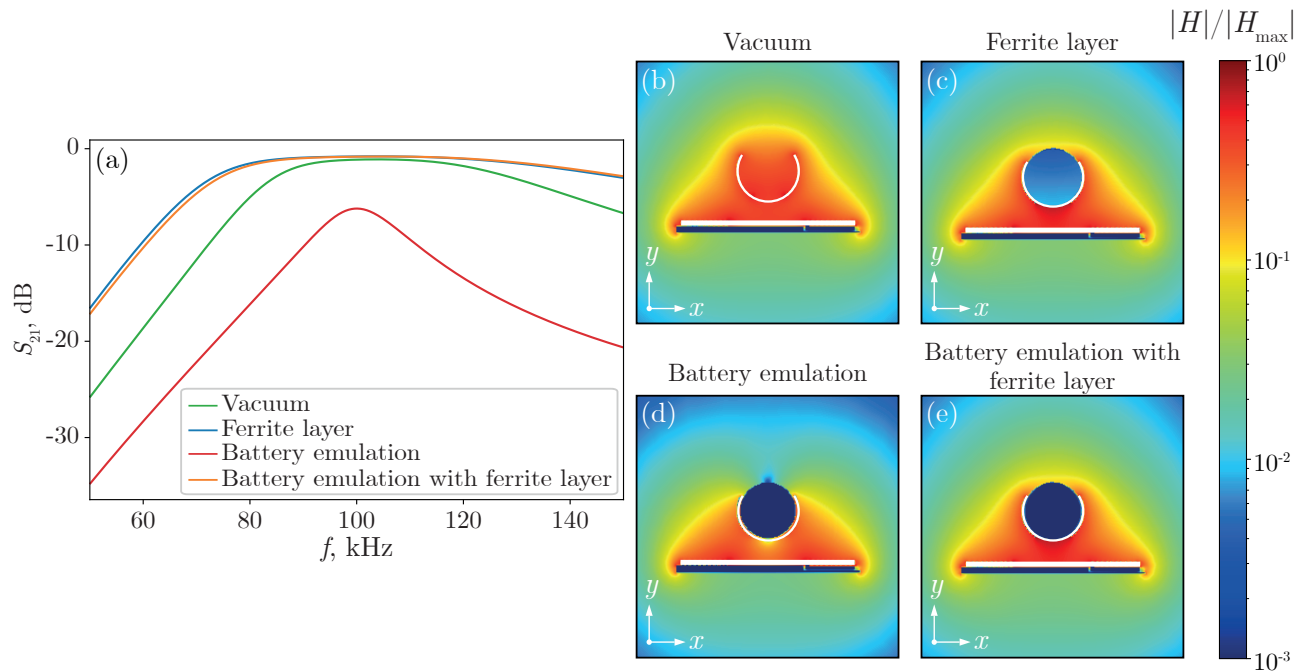


Figure S2. Comparison of numerical models with or without a ferrite layer attached to a curved receiving coil and a core-shell cylinder in the inner region of the battery outline emulating electromagnetic properties of a Li-ion cell, printed circuit boards, and wires. (a) Frequency dependencies of  $S_{21}$ -parameters for the four considered configurations. (b)-(e) Magnetic field profiles in the  $(xy)$ -plane for the following cases: (b) without both a ferrite layer and components emulation, (c) with a ferrite layer, but without components emulation, (d) without a ferrite layer, but with components emulation, and (e) with both a ferrite layer and components emulation. In all cases, the models with  $\rho = 7$  mm and  $h = 5$  mm are considered.

the magnetic field distributions and  $S_{21}$ -parameters. In particular, we consider a cylindrically bent receiving coil with curvature radius  $\rho = 7$  mm, the same coil supplied with a thin ferrite layer, the coil with a layered cylinder emulating other components of the battery, and, finally, the receiving coil with both a cylinder and a ferrite layer. The obtained  $S_{21}$ -parameters demonstrate that the presence of the cylinder deteriorates the transmission coefficient between the transmitting and the receiving coils, Fig. S2(a). Nevertheless, incorporating a thin ferrite substrate between the coil and the cylinder provides suitable magnetic shielding and considerably improves the coupling efficiency. As seen from magnetic field profiles in Fig. S2(b)-(e), when the ferrite layer is introduced, the magnetic field profiles demonstrate a more pronounced concentration between the centers of the receiving and the transmitting coils, thus increasing their coupling efficiency, Fig. S2(b,c). In turn, adding battery components to the receiving coil in the absence of the ferrite layer leads to a local decrease in the field amplitude, as shown in Fig. S2(d). Finally, the results for the model combining the presence of components and the ferrite layer [Fig. S2(e)] closely resemble those obtained for the receiving coil with a ferrite layer and without a cylinder, highlighting the efficiency of magnetic shielding.

## SUPPLEMENTARY NOTE 2. COMPARISON OF RECEIVING COILS

In this Note, we compare several potential receiving coil designs to establish the most efficient ones that can serve as starting points in further engineering optimization. We examine the following designs: the curved standard Qi receiving coil considered in the main text which covers more than a half of the battery surface [Fig. S3(a)], a combined coil consisting of two coils covering together the whole battery surface [Fig. S3(b)], and a large single coil covering

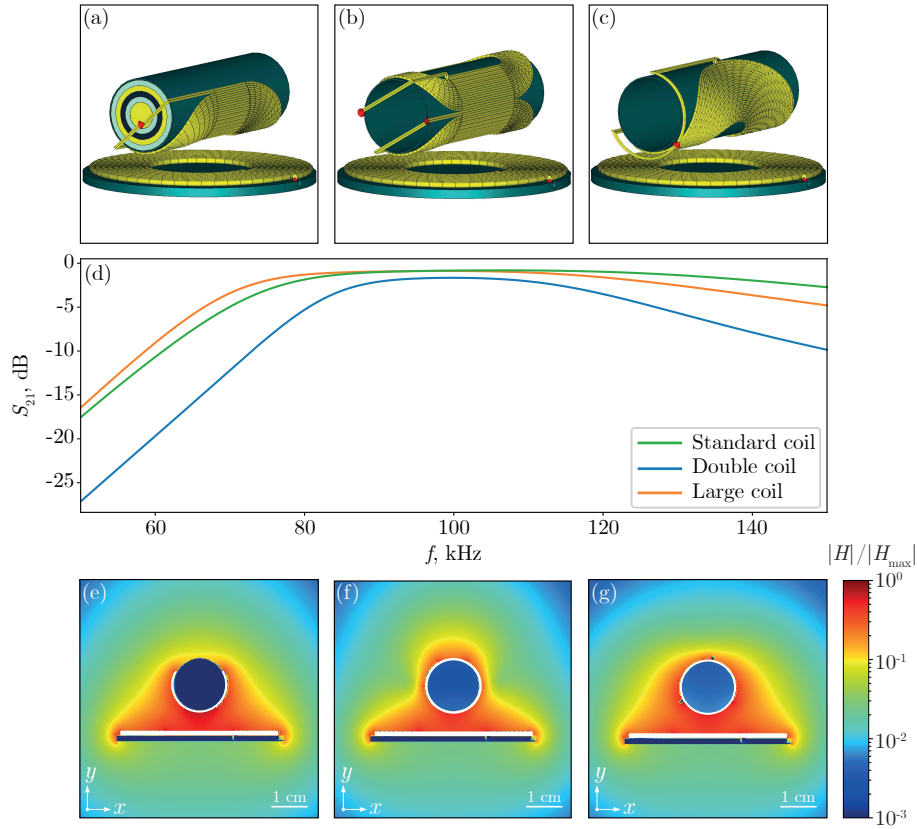


Figure S3. Comparison of three considered receiving coils designs: (a) a single coil having geometric parameters characteristic of commercial Qi coils and covering half of the AA battery surface; (b) two such coils covering full battery surface; and (c) a large single coil covering full battery surface. In all three cases, the coils are supplied with a ferrite layer. (d)  $S_{21}$ -parameters for the three considered coil types located above the transmitting coil at the height of 5 mm.

the whole battery surface [Fig. S3(c)]. As seen from frequency dependencies of  $S_{21}$ -parameters in Fig. S3(d), the double coil renders less efficient compared to the standard and enlarged coils, which demonstrate nearly the same coupling with the transmitter, with the large coil being slightly more efficient at low frequencies and the standard coil outperforming the rest in the high frequency region. A comparison of magnetic field distributions in Fig. S3(e)-(g) demonstrates that the double coil in Fig. S3(f) features two areas of pronounced magnetic field localization at the centers of two coils, in contrast to the standard coil in Fig. S3(e), while the field distribution for the enlarged coil in Fig. S3(g) resembles the one for the standard coil. Thus, counterintuitively, considering designs with several coils or maximizing the battery area covered by the receiving coil may not lead to the increase in WPT efficiency, which, as shown in Fig. 5 of the main text, remains nearly unchanged upon bending the receiving coil if compared to the standard planar receiver.

### SUPPLEMENTARY NOTE 3. EXPERIMENTAL SETUPS

To obtain the  $S$ -parameters in the kHz range, we utilize OSA103 Mini open-source platform for electrical measurements featuring amplitude and phase frequency response acquisition in the 100 Hz to 100 MHz range. As this device can only work as a scalar network analyzer able to measure the transmission coefficient  $S_{21}$  of a four-pole circuit,

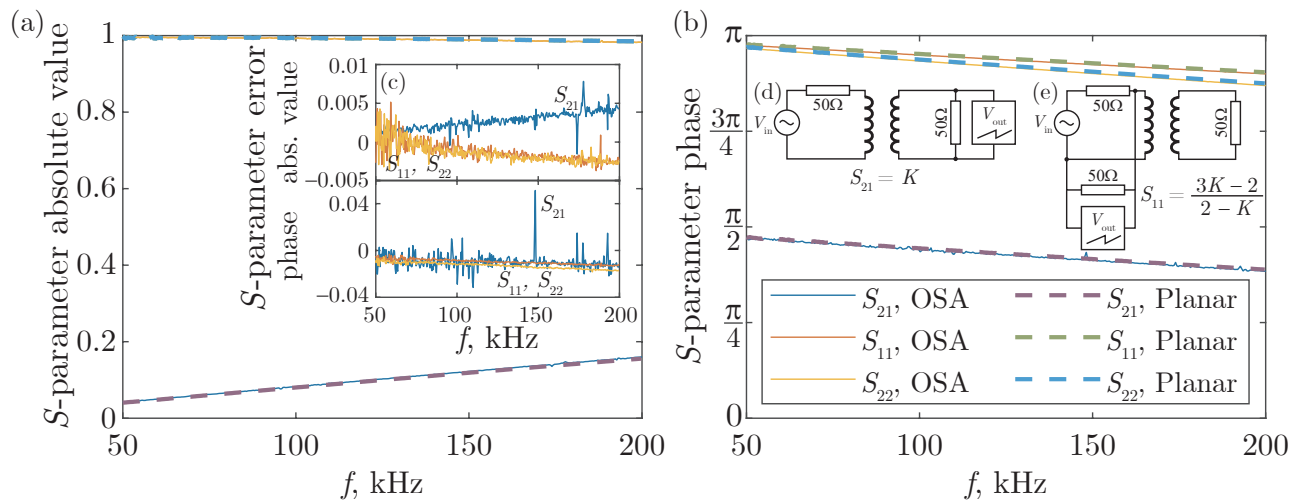


Figure S4. Amplitudes (a) and phases (b) of the reflection coefficients  $S_{11}$ ,  $S_{22}$  and transmission coefficient  $S_{21}$  parameters measured experimentally with OSA103m (solid lines) and with Planar S5048 (dashed lines.) The transmission coefficient  $S_{12}$  is equal to  $S_{21}$  by the reciprocity theorem and not shown. Inset (c) shows the differences between the  $S$  parameters measured by the aforementioned devices. Inset (d) shows the circuit used to measure  $S_{12}$  and  $S_{21}$  coefficients with the OSA103 Mini device. Inset (e) shows the circuit used to measure  $S_{11}$  and  $S_{22}$  coefficients with the OSA103 Mini device.

we use the following approach to obtain the  $S$ -parameters by indirect measurement. To obtain the transmission coefficient  $S_{21}$ , we use a setup shown in Fig. S4(d). The 50 Ohm resistors at both the input and output ports are built into the OSA103 Mini device. Preceding the measurements, a calibration was performed by replacing the coupled coils with direct connection of the input and output ports of the device by a 10-centimeter RJ142 coaxial cable. After applying the calibration, the OSA103 Mini device becomes configured in a way that the complex transmission coefficient  $K$  obtained from the device for the direct output-to-input port connection becomes unity. By connecting the transmitting coil to the output port and the receiving coil to the input port as shown in Fig. S4(d), one obtains the complex transmission coefficient  $K$ , which is equal to the transmission coefficient  $S_{21}$ . To obtain the reverse transmission coefficient  $S_{12}$ , the receiving coil is connected to the output port and the transmitting coil is connected to the input port. We note that all the circuits we obtain the  $S$ -parameters for are reciprocal, thus  $S_{12}$  is always equal to  $S_{21}$ . In our studies, we performed the measurements to obtain  $S_{12}$  as well, however, as it was equal to  $S_{21}$  in every case, we do not show it for clarity.

To obtain the reflection coefficients  $S_{11}$  and  $S_{22}$  without the use of directional couplers, which limit the accessible frequency range from the low-frequency side, we perform indirect measurements using the circuit shown in Fig. S4(e). A tee adapter is installed onto the output port of the OSA103 Mini device, with one of its outputs being connected to the input port using an RJ142 coaxial cable and the other one to the input port of the studied four-pole, which is the transmitting coil in the case shown in Fig. S4(e). The output port of the four-pole under test is terminated by a 50 Ohm dummy load. By writing down the Kirchhoff's rules for such a circuit, one can obtain an equation connecting the complex transmission coefficient  $K$  obtained from the OSA103 Mini device to the reflection coefficient  $S_{11}$  of the four-pole:

$$S_{11} = \frac{3K - 2}{2 - K}. \quad (1)$$

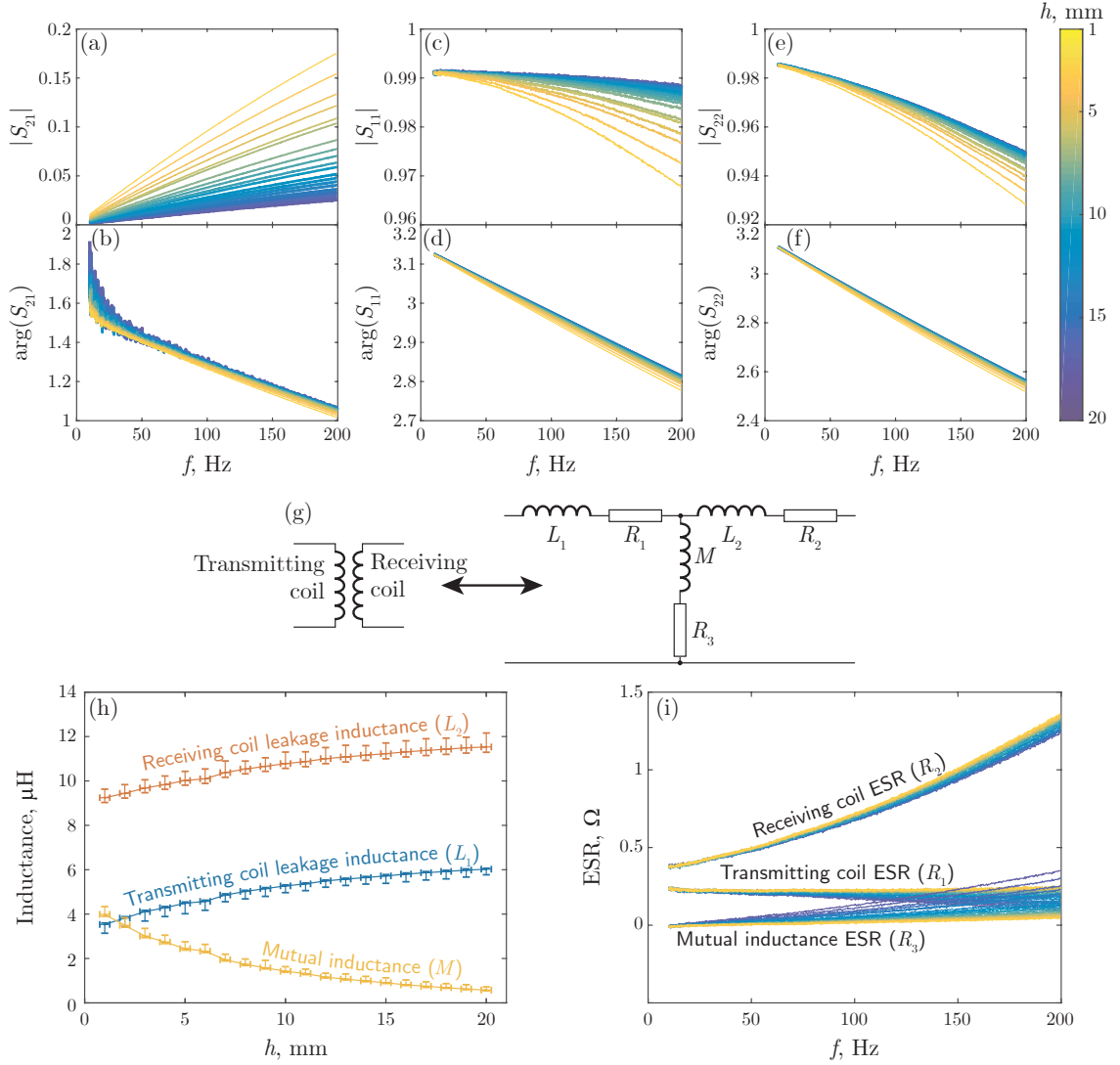


Figure S5.  $S$ -parameters of coupled transmitting and receiving coils for the distance  $h$  between the transmitting and the receiving coil varied from 1 mm to 20 mm: amplitude of the transmission coefficient  $S_{21}$  (a) and its phase (b), amplitude of the reflection coefficient from the transmitting coil  $S_{11}$  (c) and its phase (d), amplitude of the reflection coefficient from the receiving coil  $S_{22}$  (e) and its phase (f). The transmission coefficient  $S_{12}$  is equal to  $S_{21}$  by the reciprocity theorem and not shown. Equivalent circuit diagram of the coupled transmitting and receiving coils (g). Transmitting and receiving coils mutual ( $M$ ) and leakage ( $L_{1,2}$ ) inductance dependency on the distance  $h$  between the coils (h). The vertical error bars show the variation of the inductance in the 1 kHz to 200 kHz frequency range. The lines connect the average inductance values over the aforementioned frequency range. The horizontal error bars indicate the positioning error. Equivalent serial resistance (ESR) of the equivalent inductances corresponding to the transmitting and receiving coil leakage and mutual inductances, shown as a frequency dependence for the distance  $h$  between the coils varied from 1 mm to 20 mm (i).

Note that for  $K = 1$ , which corresponds to the studied four-pole being a direct connection with a 50 Ohm cable,  $S_{11} = \frac{1}{2}$ , i.e. the power is divided evenly between the 50 Ohm input impedance of the OSA103 Mini device and the 50 Ohm dummy load; while for  $K = 0$ , which corresponds to the absence of a connected four-pole,  $S_{11} = -1$ . To obtain the  $S_{22}$  reflection coefficient, the receiving coil is connected to the output port, while the transmitting coil is terminated with the dummy load.

To verify our indirect measurements, we compare the  $S$ -parameters obtained using our approach with the  $S$ -parameters obtained from the Planar S5048 vector network analyzer, which has a 20 kHz to 4.8 GHz range. The

four-pole used for this verification consisted of coupled planar transmitting and receiving coils placed 6 mm away from each other. The  $S_{11}$ ,  $S_{22}$  and  $S_{21}$  parameters obtained with both devices in the 50 kHz to 200 kHz range for two planar coupled coils are shown in Fig. S4(a,b), while the inset in Fig. S4(a) shows the difference between the values obtained by both devices.

Next, we describe the procedure used to extract the effective inductances of coupled coils. We start by obtaining the full set of  $S$ -parameters for coupled transmitting and receiving coils placed at distance  $h$  away from each other, where the transmitting coil is a planar spiral coil consisting of 10 turns of 1 mm-thick copper wire (outer diameter 42 mm, inner diameter 22 mm) placed on disk-shaped a ferrite foundation (diameter 45.5 mm, thickness 0.8 mm), and the receiver coil is a 14-turn bent  $40 \times 30$  mm<sup>2</sup> coil with the curvature radius  $\rho = 7$  mm, enclosed in an AA battery-sized photopolymer resin case and backed with a  $41 \times 28$  mm<sup>2</sup> flex ferrite sheet with 0.1 mm thickness from the interior side. The resulting  $S$ -parameters for  $h$  varied from 1 mm to 20 mm are shown in Fig. S5(a)-(f).

Imperfectly-coupled inductances can be described with the equivalent circuit shown in Fig. S5(g) [1]. We use the obtained  $S$  parameters to extract the leakage inductances  $L_1$  and  $L_2$  and their equivalent series resistances (ESR)  $R_1$  and  $R_2$ , as well as the mutual inductance  $M$  and its ESR  $R_3$ . We start by converting the  $S$ -parameter matrix to the  $ABCD$  matrix using the formulae [2]

$$\begin{aligned} A &= \frac{(Z_{01}^* + S_{11}Z_{01})(1 - S_{22}) + S_{12}S_{21}Z_{01}}{2S_{21}\sqrt{R_{01}R_{02}}}, & B &= \frac{(Z_{01}^* + S_{11}Z_{01})(Z_{02}^* + S_{22}Z_{02}) - S_{12}S_{21}Z_{01}Z_{02}}{2S_{21}\sqrt{R_{01}R_{02}}}, \\ C &= \frac{(1 - S_{11})(1 - S_{22}) - S_{12}S_{21}}{2S_{21}\sqrt{R_{01}R_{02}}}, & D &= \frac{(1 - S_{11})(Z_{02}^* + S_{22}Z_{02}) + S_{12}S_{21}Z_{02}}{2S_{21}\sqrt{R_{01}R_{02}}}, \end{aligned} \quad (2)$$

where  $Z_{01} = 50 \Omega$  is the source output impedance,  $Z_{02} = 50 \Omega$  is the load impedance,  $R_{01} = \text{Re } Z_{01}$  and  $R_{02} = \text{Re } Z_{02}$ . Next, we use the  $ABCD$  matrix for a four-pole T circuit [3]:

$$\begin{aligned} A &= 1 + \frac{Z_1}{Z_3}, & B &= Z_1 + Z_2 + \frac{Z_1Z_2}{Z_3}, \\ C &= \frac{1}{Z_3}, & D &= 1 + \frac{Z_2}{Z_3}, \end{aligned} \quad (3)$$

where

$$Z_1 = i\omega L_1 + R_1, \quad Z_2 = i\omega L_2 + R_2, \quad Z_3 = i\omega M + R_3. \quad (4)$$

Combining Eqs. (2) to (4), we obtain a closed system that expresses the leakage and mutual inductances and the corresponding ESR through the experimentally-measured  $S$  parameters. Solving these equations for each frequency yields the values shown in Fig. S5(h,i). Note that the inductances do not demonstrate any significant change with frequency, therefore we show them in Fig. S5(h) as dots with error bars that correspond to their variation in the whole 1 kHz to 200 kHz range. They do, however, change significantly depending on the distance  $h$ . We also note that the self-inductances are almost constant for all distances. The transmitting coil self-inductance  $L_{\text{Tx}} = L_1 + aM \simeq 7 \mu\text{H}$ , where  $a = 10/14$  is the winding turns ratio, while the receiving coil self-inductance  $L_{\text{Rx}} = L_1 + M/a \simeq 12 \mu\text{H}$ . In contrast, the resistances shown in Fig. S5(i) do depend on frequency, while their dependence on the distance between the coils is weak. The apparent increase of the mutual inductance ESR  $R_3$  at larger distances may be contributed to absorption of the stray ac magnetic field by surrounding objects as well as the magnetic field screening by the ferrite

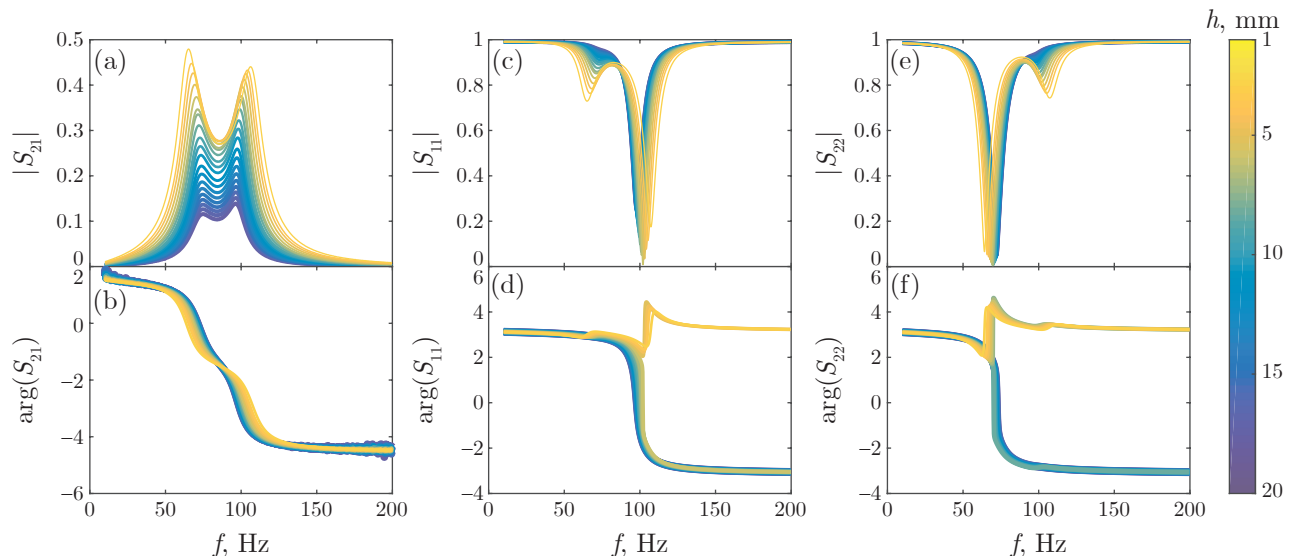


Figure S6.  $S$ -parameters of coupled serial contours for the distance  $h$  between the transmitting and the receiving coil varied from 1 mm to 20 mm: amplitude of the transmission coefficient  $S_{21}$  (a) and its phase (b), amplitude of the reflection coefficient from the transmitting coil  $S_{11}$  (c) and its phase (d), amplitude of the reflection coefficient from the receiving coil  $S_{22}$  (e) and its phase (f). The transmission coefficient  $S_{12}$  is equal to  $S_{21}$  by the reciprocity theorem and not shown.

sheet becoming less efficient.

#### SUPPLEMENTARY NOTE 4. PROTOTYPE SCHEMATICS

Our prototype of the AA battery with Qi-compatible wireless charging exploits a Li-ion cell and a number of dc-dc converters. Its main functional blocks are shown in Fig. S7, while the complete electric circuit diagram is shown in Fig. S8. To convert the voltage of the Li-ion cell to the 1.5 V output (marked as +1.5V power terminal on the circuit diagram), a switching dc-dc converter consisting of a driver chip U102, inductor L101, feedback network consisting of resistors R103 and R104 and smoothing capacitors C102–C104 is utilized. The Li-ion cell BT101 is connected to the input of the aforementioned switching dc-dc converter.

Charging of the cell involves receiving of ac magnetic field with the receiving coil operating near the resonance of the input tank circuit, rectification of the resulting voltage yielding 5 V to 8.5 V dc (marked as +8V power terminal on the circuit diagram), depending on the placement of the receiving coil respective to the transmitter, transforming the resulting voltage to 5 V dc (marked as +5V power terminal on the circuit diagram) with a switching dc-dc converter, and finally transforming the 5 V dc into either 4.2 V in the constant voltage (CV) mode or into 100 mA current in the constant current (CC) mode, suitable for charging the Li-ion cell BT101, using the Battery charger IC. The receiving tank circuit consists of the receiving coil L1 and the tuning capacitors C2–C6 connected in parallel adding up to a total capacitance of 270 nF. The rectifier is a full-bridge circuit, with the positive half of the bridge consisting of Schottky diodes D1 and D2, and while the body diodes of the MOSFETs Q2 and Q3 act as the negative half of the bridge. The capacitors C8 and C9, connected in parallel, smooth the output voltage of the rectifier. The 5V switching dc-dc converter consists of a driver chip U3, inductor L2, feedback network consisting of resistors R7 and R8, bootstrap capacitor C14 and smoothing capacitors C15–C18, which are connected in parallel, as well as C20. The battery charger



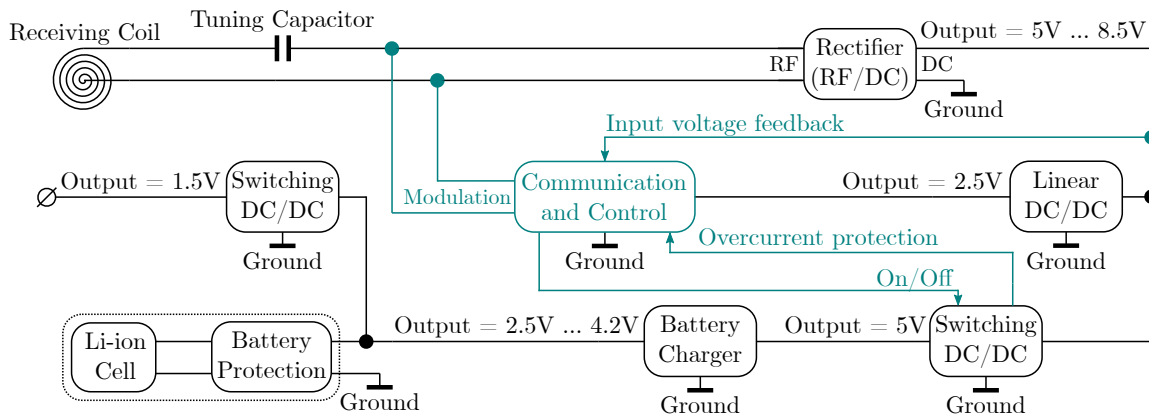


Figure S7. Functional block diagram of the prototype.

consists of a dissipative voltage–current limiter U101, a CC current programming resistor R101, a charge indication LED D101 with a current-limiting resistor R102, as well as the smoothing capacitor C101. The output of the battery charger is connected to the Li-ion cell BT101.

To establish the receiver-to-transmitter feedback loop, a Communication and Control circuit, powered by a 2.5 V linear dc-dc converter (its output is marked as +2V5 power terminal on the circuit diagram), monitors the output voltage of the rectifier as well as the current consumed by the 5 V dc-dc converter, and uses capacitive load modulation of the receiving tank circuit to transmit control error (CE) packets to the transmitter that request it to increase or decrease the signal strength. The linear dc-dc converter consists of a current-limiting resistor R1, a linear shunt regulator U1, as well as two smoothing capacitors C10 and C11, which are connected in parallel. The Communication and Control circuit consists of a microcontroller unit (MCU) U2, two resistors R4 and R5 and a smoothing capacitor C13 making up a resistive voltage divider, and a current sense resistor R2 bypassed by a smoothing capacitor C12, which connects the ground terminal GND, used by the receiver and the Communication and Control circuit, to the ground terminal GNDPWR, which is shared by all the power consumers. The capacitive load modulation of the input tank circuit is performed by two MOSFETs Q1 and Q4 connecting the bypass capacitors C1 and C7 to the input tank circuit, increasing its resonant frequency by almost an order of magnitude. This leads to a significant change in the supply current consumed by the transmitter, which it monitors and uses to read the CE packets and change the output power accordingly.

All electronic components of the prototype are assembled on two separate two-sided flex printed circuit boards (PCB), that are connected with wires. The components with reference designator numbers 1–99 (e. g. R4 or C20) are mounted on the first PCB, while those with numbers starting from 101 (e. g. U102) are mounted on the second one.

- 
- [1] A R Daniels, *Introduction to electrical machines* (Macmillan, 1976).  
 [2] Dean A Frickey, “Conversions between  $S$ ,  $Z$ ,  $Y$ ,  $H$ ,  $ABCD$ , and  $T$  parameters which are valid for complex source and load impedances,” *IEEE Transactions on microwave theory and techniques* **42**, 205–211 (1994).  
 [3] Vincent F Fusco, *Microwave circuits: analysis and computer-aided design*, 3rd ed. (Prentice-Hall, 1987).

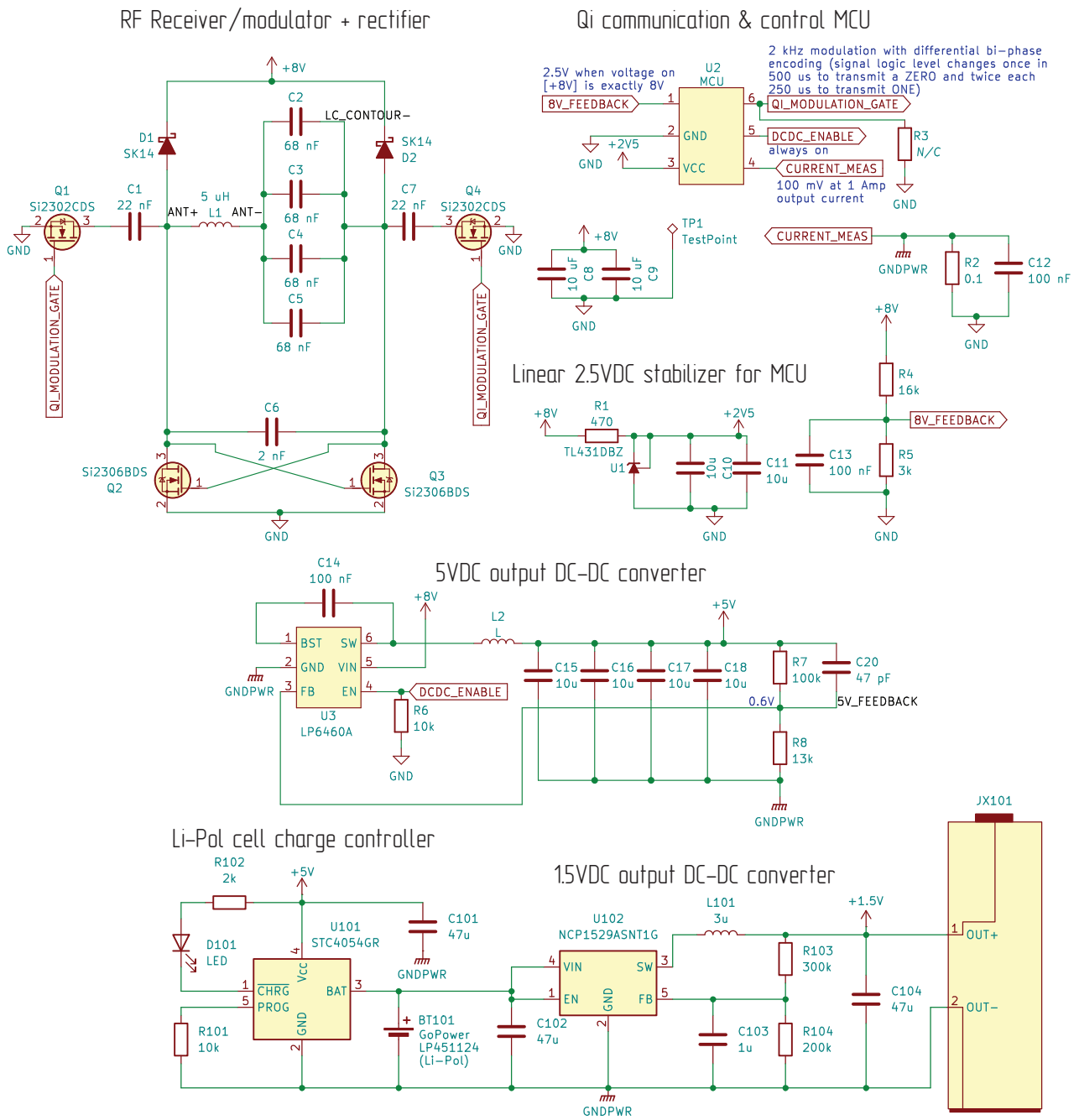


Figure S8. Complete electric circuit diagram of the prototype.